Received:Added at production | Revised:Added at production | Accepted: Added at production
DOI: xxx/xxxx

ARTICLE TYPE: Research paper

Engineering Reports

Characterization of IGV-Rotor Interactions in a Pre-Whirl Axial Fan

Adel Ghenaiet *[1] |

[1]Laboratory of Energetic Mechanics and Conversion Systems, Faculty of Mechanical Engineering, University of Science and Technology, Houari Boumediene, BP 32 El-Alia, Bab-Ezzouar, 16111, Algiers, Algeria

Correspondence
* Adel Ghenaiet,
Laboratory of Energetic Mechanics and Conversion Systems, Faculty of Mechanical Engineering, University of Science and Technology, Houari Boumediene, BP 32 El-Alia, Bab-Ezzouar, 16111, Algiers, Algeria
Email: ag1964@yahoo.com

Funding Information
Project Name: XXXXXXXX
Grant/Award Number: XXXXXXXX

Abstract

The main goal of this study is to determine the aerodynamic performance and to characterize unsteady flows in a high-speed high-reaction pre-whirl axial flow fan. The pressure waves' main diametrical modes where two blades interact with two vanes and their sequences are predicted. There are mainly two mechanisms of IGV-rotor interactions identified; the first is attributed to the potential effect whereas the second is due to the wake-blade interaction and the advection of wake mixing into the blades' passages. Both effects are dependent on the circumferential positions of blades and the axial inter-distance between IGV and rotor. The time mode analyses of pressure fluctuations recorded from different monitor points are determined and the frequencies of prevailing modes and those related to the vortical flow structure through the components are also identified. The understanding of vanes and blade rows interactions at various axial inter-distances is an important step in determining the beneficial and detrimental effects on the design of high performance axial fan stage.

KEYWORDS

Pre-whirl axial fan, Steady and unsteady flows, Aerodynamic performance, IGV-rotor interactions, Pressure fluctuations, ANSYS-CFX solver

1 | INTRODUCTION

The flow in a high performance axial fan stage is inherently unsteady because of the interactions due to relative motion between the preceding Inlet Guide Vanes (IGV) and rotating blades. This has been regarded as the primary source of pressure fluctuations which in addition to noise and vibrations introduce unfavourable changes in performance in terms of aerodynamic efficiency, operating stability and range. Earliest investigation on Rotor/Stator or Stator/Rotor interaction, known as RSI phenomena, was due to Kemp et al. [1], and since many past researchers have undertaken such studies [2-6]. The dominant causes of such unsteadiness are attributed to the wake/blade interaction in which wakes produced by upstream stator (IGV) are swept downstream into the next rotor row, followed by the vortex

Received:Added at production | Revised:Added at production | Accepted: Added at production
DOI: xxx/xxxx

shedding at trailing edges added to the potential effect in which the pressure field associated with the leading edge of a rotor sweeps past the trailing edge of an upstream vane (stator) [2, 7]. Adamczyk et al. [8] have described the wake mixing within a rotor passage and the tendency of stator wake to drift toward the pressure side of a downstream rotor. As the RSI phenomena do change the real flow; In case of an axial compressor the wakes at rotor exit fluctuate strongly so that the incidence angle to the next stator is higher and the flow turning is higher too in the following blade [9]. Experimental studies of wake/rotor interactions were performed by Kerrebrock and Mikolajczak [10] for the compressors and by Binder et al. [11] and Hodson [12] for the turbines. Hsu and Wo [13] carried out an experimental investigation on unsteady interactions in a large-scale low-speed 1.5-stage axial compressor, followed a numerical study by Lee and Feng [14]. In their two-part papers, Mailach et al. [15, 16] presented detailed experimental investigations of unsteady blade-row interactions in a low-speed research compressor and discussed the effect of blade-row clocking on the unsteady profile pressures. Later, Jia et al. [17] investigated numerically the same compressor and compared with experiments. The study of the different aspects of RSI phenomena may help in improving the design of high performance axial fan stages and reduce noise emission. Tsuchiya et al. [18] attempted to predict RSI in a high-speed fan stage acoustically based on Unsteady Reynolds-Averaged Navier-Stokes equations (URANS) to acquire the pressures pulsations induced by wakes. Also, Kodama et al. [19] performed URANS analyses for the effects of axial spacing and vane geometry on the unsteady pressure fluctuations. More recently, there are typically the works of Oro et al. [20], who introduced an URANS modelling for the flow in an axial fan stage of 13 vanes in IGV and 9 blades in rotor, and their focus was on RSI and the influence of inter-distance. They showed that the deterministic kinetic energy could be used effectively in analyzing such unsteady phenomena. Later on, for the same axial fan stage, Oro et al. [21] developed an experimental open-loop facility to obtain a physical description of the flow, where exhaustive analyses of measured wakes provided a comprehensive description of both wake-transport phenomena and RSI mechanisms. The unsteadiness associated to the wakes convected through the passages of the same low-speed axial fan stage was further studied by Vega et al. [22] based on LES simulations to resolve the largest scales of the vortical motion related to vortex shedding. The numerical modelling was able to reproduce accurately the unsteady phenomena that occur inside the axial fan; specifically the chopping mechanisms and the periodic interactions of the coherent turbulent structures were described and compared with experiments.

The present contribution paper focuses on studying RSI phenomena in a high-speed high-reaction pre-whirl axial fan stage, operating at a variable speed, shown in Fig. 1. The main data are also provided in Table 1. First, the aerodynamic performances were determined at different speed and including the effect of axial inter-distance. Second the unsteady flow simulations were carried out to predict the static pressure fluctuations at different monitor points. As results, the sequences of mode shapes of RSI are well illustrated for this high-speed axial fan stage in terms of frequencies and amplitudes base on Fast Fourier Transform (FFT).

Received:Added at production | Revised:Added at production | Accepted: Added at production
DOI: xxx/xxxx

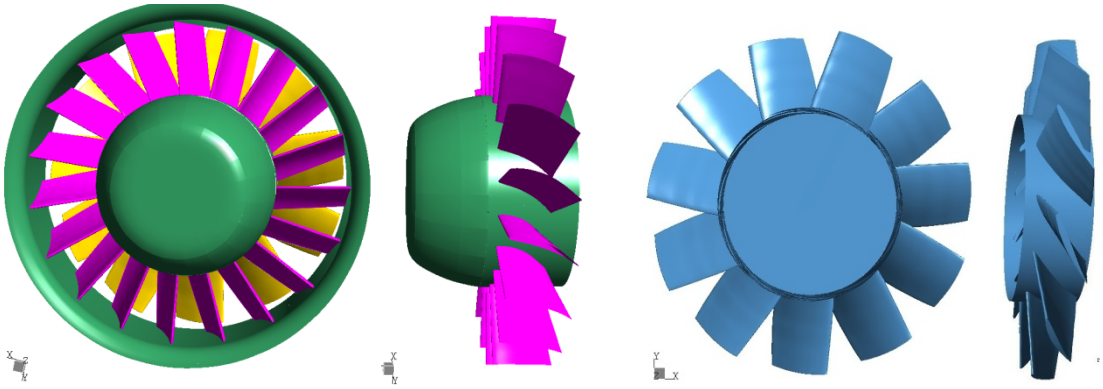

(a) **(b)**

Figure 1 Axial fan stage**:** a) IGV; b) Rotor

Table 1 Axial fan stage geometry parameters

Parameter	IGV	Rotor
Number of vanes/blades	19	11
Tip diameter (mm)	388	386
Hub diameter (mm)	214.5	214.5
Tip clearance (mm)	-	1
Blade chord at tip (mm)	75	75
Blade chord at hub (mm)	65	90
Stagger angle at tip (deg)	22	63
Stagger angle at hub (deg)	30	52
Camber angle (deg)	30	20
Blade thickness ratio (t/l) (%)	10	10

2 | CFD MODEL

URANS equations in terms of continuity, momentum and energy are given as follows:

$$\frac{\partial \rho}{\partial t} + \frac{\partial}{\partial x_j}\left(\rho U_j\right) = 0 \quad (1)$$

$$\frac{\partial}{\partial t}\left(\rho U_i\right) + \frac{\partial}{\partial x_j}\left(\rho U_i U_j\right) = -\frac{\partial p}{\partial x_i} + \frac{\partial}{\partial x_j}\left[\tau_{ij} - \rho\overline{u_i u_j}\right] + S_M \quad (2)$$

$$\frac{\partial}{\partial t}(\rho H) - \frac{\partial P}{\partial t} + \frac{\partial}{\partial x_j}\left(\rho U_j H\right) = \frac{\partial}{\partial x_j}\left(\lambda\frac{\partial T}{\partial x_j} + \rho\overline{u_j h}\right) + \frac{\partial}{\partial x_j}\left[U_i\left(\tau_{ij} - \rho\overline{u_i u_j}\right)\right] + S_E \quad (3)$$

Where $\overrightarrow{S_M} = -2\vec{\Omega} \times \vec{U} + \vec{\Omega} \times (\vec{\Omega} \times \vec{r})$, $\vec{\Omega}$ rotational velocity (rad/s), $\vec{U}$ relative flow velocity, τ_{ij} is the molecular stress tensor and $\rho\overline{u_i u_j}$ is the Reynolds stresses. $H = h + \frac{1}{2}U^2 + k$ is the total enthalpy, S_E is the energy source term, k is the turbulent kinetic energy and λ is the thermal conductivity. k-ω based SST (Menter [23]) turbulence closure model is used owing to reliability in analyzing RSI and good revelation of pressure oscillation [24].

2.1 Solver

The flow field through this axial fan stage extended upstream and downstream is solved by means of the code ANSYS-CFX [25] which uses the finite volume method. The governing equations are integrated over each control volume defined by joining the centres of edges and

Received:Added at production | Revised:Added at production | Accepted: Added at production
DOI: xxx/xxxx

the element centres surrounding each node. Gauss divergence theorem is applied to convert the volume integrals involving divergence and gradient operators to the surface integrals. Volume integrals are discretized within each element sector and accumulated to the control volume to which the sector belongs, whereas the surface integrals are discretized at the central integration points of each surface segment. After discretizing the volume and surface integrals, the integral equations become:

$$V\left(\frac{\rho-\rho_0}{\Delta t}\right)+\sum_{ip}\dot{m}_{ip}=0 \tag{4}$$

$$V\left(\frac{\rho U_i-\rho^0 U_i^0}{\Delta t}\right)+\sum_{ip}\dot{m}_{ip}(U_i)_{ip}=\sum_{ip}(P\Delta n_i)_{ip}+\sum_{ip}\left(\mu_{eff}\left(\frac{\partial U_i}{\partial x_j}+\frac{\partial U_j}{\partial x_i}\right)\Delta n_j\right)_{ip}+\overline{S_{U_i}}V \tag{5}$$

$$V\left(\frac{\rho\varphi-\rho^0\varphi^0}{\Delta t}\right)+\sum_{ip}\dot{m}_{ip}(\varphi)_{ip}=\sum_{ip}\left(\Gamma_{\text{eff}}\frac{\partial\varphi}{\partial \text{x}_\text{j}}\Delta n_j\right)_{ip}+\overline{S_\varphi}V \tag{6}$$

Where $\dot{m}_{ip}=(\rho U_j\Delta n_j)_{ip}$, Δt is the time step, Δn_j is the discrete outward surface vector, ip denotes an integration point and (°) refers to an old time level. Where $\mu_{eff}=\mu+\mu_\tau$ and $\Gamma_{eff}=\Gamma+\Gamma_\tau$ are successively the effective viscosity and effective diffusivity. The solution field parameters are stored at the mesh nodes and by using finite-element linear shape function in terms of parametric coordinates $\varphi=\sum_{i=1}^{N_{node}}N_i\varphi_i$ the approximation of all flow properties, gradients and diffusion terms at the integration points are obtained. To prevent the pressure field oscillations as a result of the non-staggered collocated grid arrangement, a coupled solver solves the flow equations as a single system. The high resolution scheme is used for the advection terms in the equations of momentum and the turbulent model casted in the form $\varphi_{ip}=\varphi_{up}+\beta\nabla\varphi\Delta\vec{r}$ [25], where φ_{up} is the value at upwind node and $\vec{r}$ is the vector from the upwind node to the point ip. For the high resolution β is computed to be less or equal to 1.

For the steady state simulations the solver applies a false time step as a means of under-relaxing the equations as they iterate towards the final solution. This can be adjusted as an internally calculated physical time scale based on the domain geometry, boundary conditions and flow conditions, or a local time scale factor in different regions and finally a fixed value over the entire flow domain equal to $1/\omega$ (ω rotational speed). This last option was selected in the steady flow computations based on the high resolution scheme for the advection terms while the convergence residual was set at a value of 10^{-6}.

For unsteady flow computations the high resolution scheme [25] operates as a second order backward Euler scheme (shown as below is robust and implicit) wherever and whenever possible and reverts to the first order backward Euler scheme when is required to maintain a bounded solution.

$$\frac{\partial}{\partial t}\int_V\rho\varphi dV=V\frac{1}{\Delta t}\left(\frac{3}{2}(\rho\varphi)-(\rho\varphi)^0+\frac{1}{2}(\rho\varphi)^{00}\right) \tag{7}$$

During the computations, at each time step the convergence is controlled by the minimum and maximum number of iterations, but the maximum number of iterations per a time step may not always be reached if the residual target level is achieved first. The solver performs a number of 15 iterations for each time step to reach a residual inferior to a value of 10^{-5}. The transient rotor/stator interface is used to account for the transient interactions between the IGV vanes and rotor blades-row.

The time step has to be small enough to get the necessary time resolution depending on the speed of rotation. However, to have a good resolution of unsteady RSI the time step is chosen to satisfy all the time periods characterizing the aerodynamic operation of this axial fan stage.

Received:Added at production | Revised:Added at production | Accepted: Added at production
DOI: xxx/xxxx

For two blade-rows (vanes and rotor blades) of N_1 vanes and N_2 blades, the different characteristic time scales are estimated as follows:

- The necessary time to accomplish one rotor round is $\Delta t_{round} = 60/N$
- The apparent blade passing period of the row $(3-\mathrm{i})$in the row (i) is $\Delta t_i = \Delta t_{round}/N_{3-i}$ $\mathrm{i} = 1{,}2$, where $\mathrm{N_{3-i}}$ is the blade number of row $(3-\mathrm{i})$
- The necessary time to cover geometrical coincidence (the space-time period of two blade rows (stator and rotor)) is given by $\Delta t_{min} = \Delta t_{round} GCD(N_i, N_{3-i})/N_i N_{3-i}$ where $\mathrm{GCD(N_i, N_{3-i})}$ is the greatest common divisor of the two blade number N_i and N_{3-i}..

  For the IGV and rotor blades $T_{min} = \frac{T_{round} GCD(19,11)}{19*11} = 0.00478\Delta \mathrm{t_{round}}$. When the fan operates at the nominal point (N= 6000 rpm, m= 5.06 kg/s) $\Delta t_{round} = 60/N = 0.01$ s, thus $T_{min} = 47.84\ \mu s$ equivalent to 1.72 deg and represents the upper limit of the time to be used. However, to resolve the high frequencies, the computational time step should correspond to a rotation less or equal 1.5 deg as stated in some references such as [26], and thus the time step was set at $41.66\ \mu s$ and for one round the total time is equal to $10\ ms$.
The transient relative motion on each side of the general grid interface (GGI) connection is simulated and the interface position updated at each time step.

2.2 Mesh generation

The geometry of the real machine was reproduced by means of a coordinate measuring tri-optic machine. The Hexahedral mesh blocks were distributed to have fine meshing near the leading edge and trailing edge and the hub and shroud of vane and blade. refinements around the vanes and blades were made for 15 mesh lines nearest the wall and with minimum volume distortion to get accuracy for the boundary layers resolution. A refinment to the tip clearance of 15 mesh lines to capture the details of leakage flow. A minimum number of nodes was secured inside the boundary layers so that kω-SST turbulence [23] can be used. An automatic wall function control [23] allowed to switch from the wall function for $20<y^+<100$ and the low reynolds model for $y^+ < 2$. Based on simulations at the nominal operating point (N=6000 rpm, m=5.06 kg/s), the first layer of nodes from a wall is estimated by $\Delta y = y^+\mu/\rho V_t$, where $V_t = V_\infty \sqrt{C_f/2}$ and $C_f = 0.026 Re_c^{-1/7}$ [27]for Reynolds number $Re_c = \rho V_\infty c/\mu$ based on vane/blade chord. $\Delta y = y^+\sqrt{80} C_{av} Re_{C_{av}}^{-0.92}$, where the chord $c_{av} = 89$ mm and the maximum flow velocity equal to $150\ \mathrm{m/s}$. For y^+ about 2 the nearest meshline is about 5 μm. The study of grid size dependency was conducted at the nominal operating conditions for five meshes of the runner blade, revealed stabilized steady state performance for a total mesh size of 2.75 million nodes For the complete circumerential components of this axial fan stage**.** Figure 2 presents part views of used meshes per sectors.

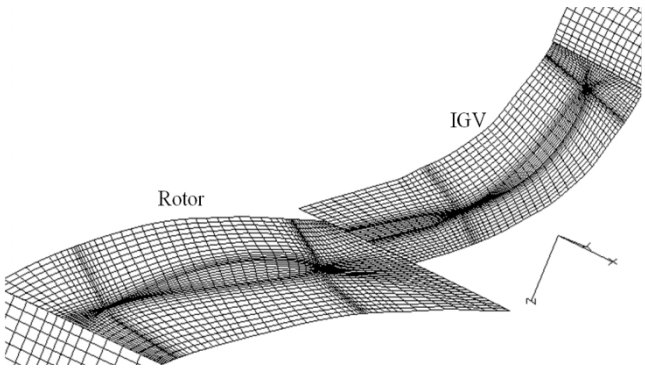

(a)

Received:Added at production | Revised:Added at production | Accepted: Added at production
DOI: xxx/xxxx

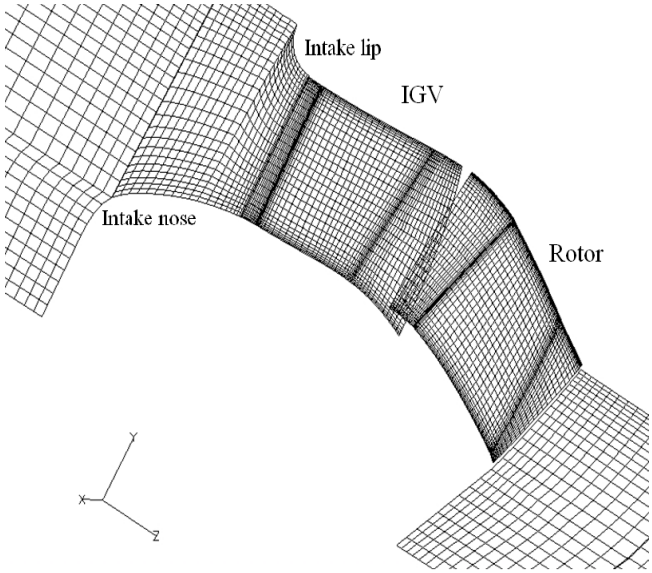

(b)

Figure 2 Grids of IGV and rotor blades: a) Mid-span; b) Meridional plan

2.3 Boundary conditions

As boundary conditions a total pressure and temperature imposed at the inlet, while a static pressure at the outlet which was varied to sweep the totality of flow range for each rotational speed. On the rough walls a no-slip boundary condition was applied. Upstream IGV free stream turbulence intensity $Tu = \frac{(2k/3)^{0.5}}{V}$ is set where the representative velocity is that at inlet. The inlet turbulence intensity was set at 5 % and the length scale equal to 0.1 times the guide vane span, whereas the turbulent viscosity was evaluated using Wilcox's model [28].

3 | STEADY FLOW RESULTS

First, the steady flow simulations used the stage interface for the aerodynamic performance computation. On the other hand, the frozen interface produced the steady solution to multiple frames with some account of interaction between them, which served in the flow structures characterization.

3.1 Performance maps

From the steady solution with a circumferential averaging of fluxes through the interface using the stage interface (mixing plan) the total-total isentropic efficiency and pressure rise were computed base on mass flow averaging of total pressure and temperature with respect to inlet and outlet of the computational domain. The fan stage has a large range of operation (Fig. 3), as it is characterized by a mass flow rate from 1.5 kg/s to 10 kg/s and a pressure rise from 100 mm to 950 mm of water column when the rotational speed varies from 2500 rpm to 8000 rpm. The design (nominal) point corresponds to the maximum total-total isentropic efficiency of 74% (Fig 4), obtained for the mass flow rate of 5.06 kg/s and the speed of rotation equal to 6000 rpm.

Received:Added at production | Revised:Added at production | Accepted: Added at production
DOI: xxx/xxxx

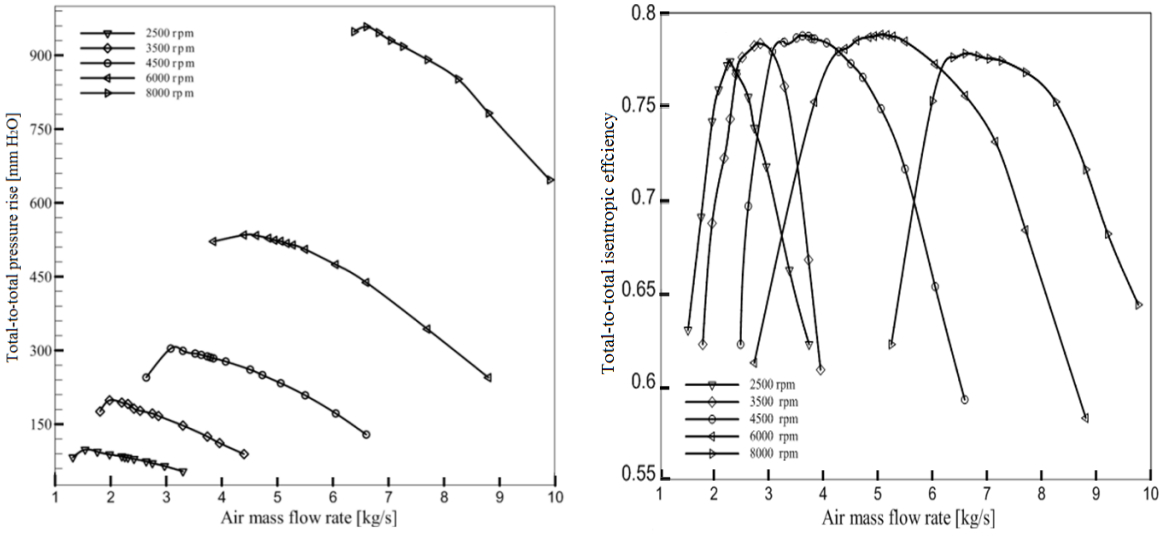

(a) **(b)**

Figure 3 Aerodynamic performance: a) Pressure rise, b) Total-total isentropic efficiency

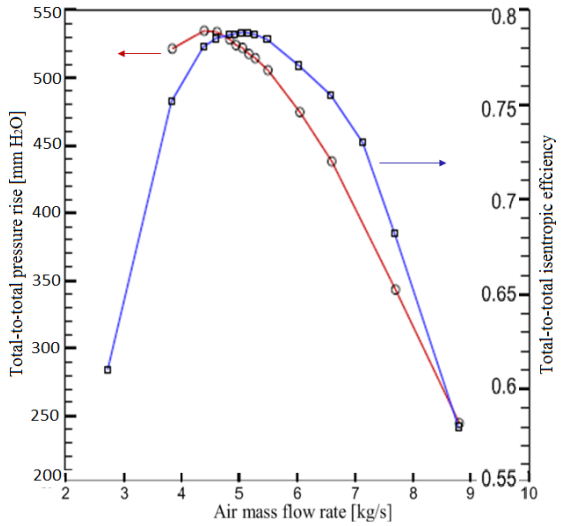

Figure 4 aerodynamic performances at the nominal speed

3.2 Flow structures

With the frozen interface simulations at the nominal point (*N*=6000 rpm, m=5.06 kg/s), the relative position between the stationary and rotating components is taken into account. The calculations were started with five given relative position (Fig. 5) of an angle 4.73 deg imposed to simulate the pseudo clocking effect. The first orientation corresponds to first vane (IGV) trailing edge facing the rotor blade leading edge.

Received:Added at production | Revised:Added at production | Accepted: Added at production
DOI: xxx/xxxx

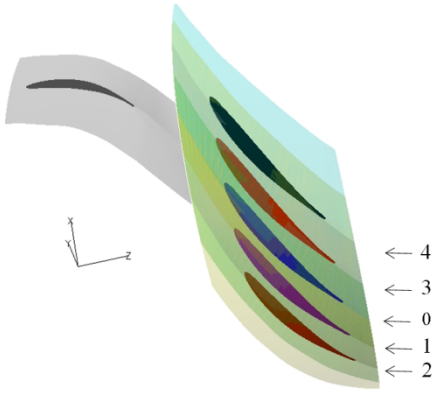

Figure 5. Relative rotor blade positions

Figure 6(a) show that the flow field is characterized by high flow velocities reaching 200 m/s conformed to different clocking positions, where parts of IGV wakes are convected through the blade passages while the flow incidence and station point around the blade are affected. Further flow complexity occurs in the tip clearance where the leakage around develops into a vortex and mixes out with the annulus wall boundary layer. Figure 6(b) depicts variations in the static pressure, which is more significant at the fore of rotor blade, and diffusion is remarkably influenced by the blade position. Downstream rotor blade the flow is influenced by the back-pressure from the rotor step and the flow rotation and diffusion continues further.

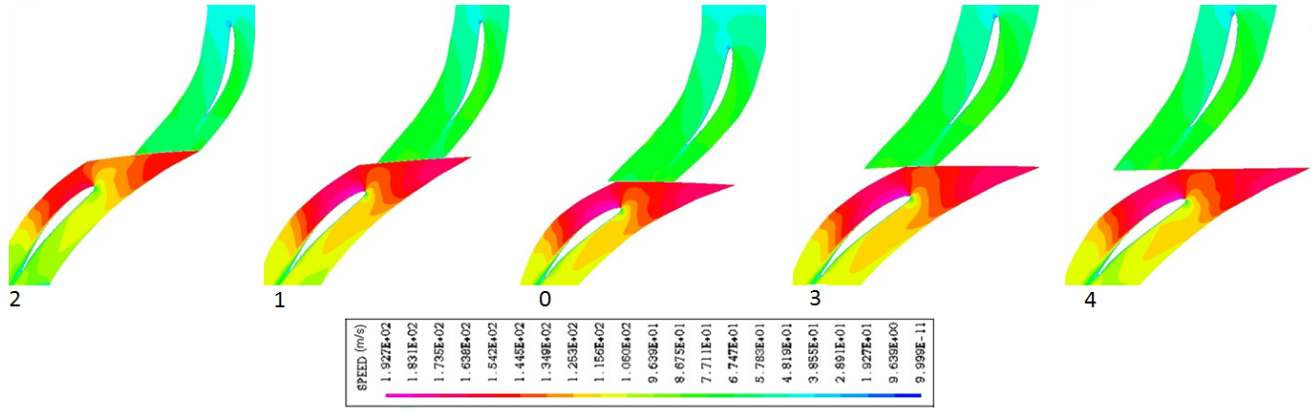

(a)

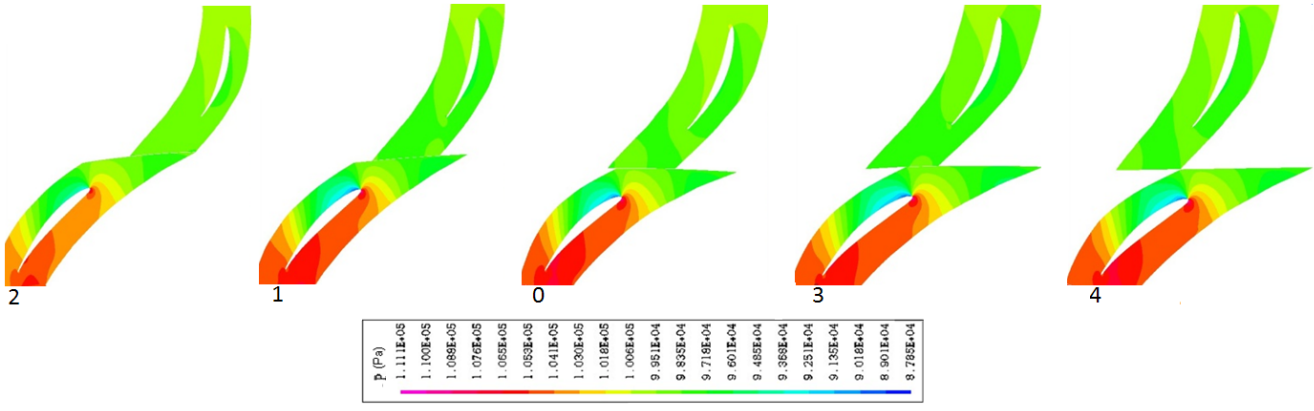

(b)

Figure 6 Flow properties at mid-span for positions 0, 1, 2, 3, 4: a) Velocity; b) Static pressure

Received:Added at production | Revised:Added at production | Accepted: Added at production
DOI: xxx/xxxx

Figure 7 depicts the evolutions of static pressure around IGV vane and rotor blade with different positions of frozen-rotor. The distribution of static pressure on IGV blade looks in some extent similar for all positions expect there are small variations at trailing edge. For the rotor there are noticeable variations in pressure (loading) on both sides of blade which become clearer beyond 60 % of chord and more towards the blade trailing edge from both sides due to wakes interaction. The wakes of different vanes traverse differently the blades passages and are chopped into segments by the downstream blade row, and do not periodically envelop the rotor blades and behave as a negative jet impinging on the leading edge of blades, hence altering the inlet flow angle and the boundary layers and subsequently the aerodynamic loading of blades is drastically affected.

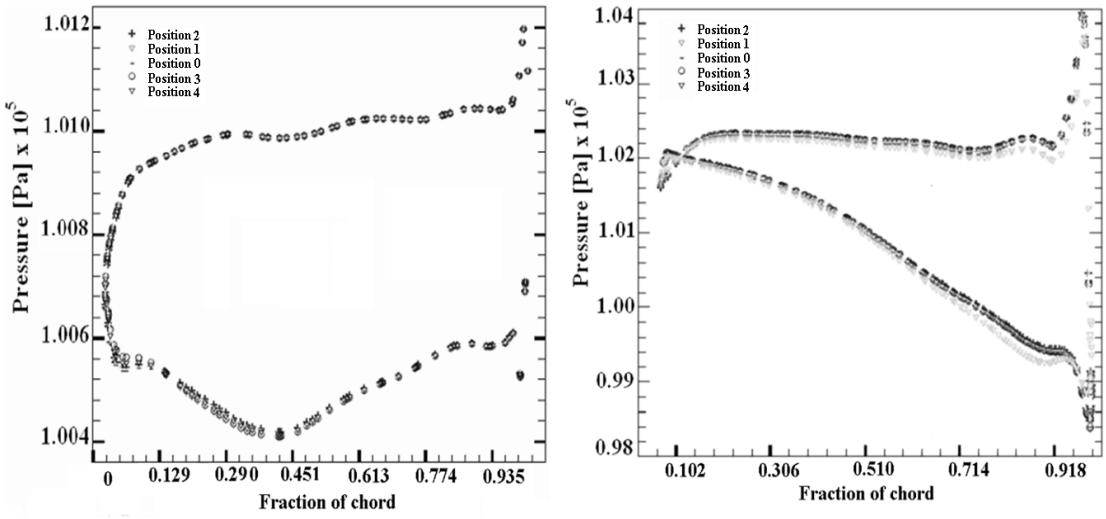

(a) **(b)**

Figure 7 Static pressure over mid-span: a) IGV (left), b) rotor blade (right)

In this IGV-rotor configuration with rotor blades designed for free vortex distribution to ensure a radial equilibrium flow, there is a swirl velocity at IGV exit giving a spanwise vortex-free pre-rotation which is balanced by an axial velocity obeying the equation of radial total pressure variation. From hub to mid-span the axial velocity concentration tends to reduce the flow incidence, while from the mid-span to tip the blockage tends to increase incidence. At a reduced mass flow, the higher angle of attack is responsible for increasing the aerodynamic loading towards the blade tip, but it is compensated by the high losses due to the suction side flow. The radial distribution of axial velocity at rotor exit is related to the axial blockage imposed at IGV trailing edge which becomes more at low flow rate. Figures 8 present the subsequent evolutions of total pressure and entropy at a half chord distance downstream of rotor blade and for three operating conditions of the fan stage. It is obvious that the most significant variations in velocity profiles appear in the regions at 15 % span near the hub and 75 % span from the casing, which are relating where high losses are present.

Received:Added at production | Revised:Added at production | Accepted: Added at production
DOI: xxx/xxxx

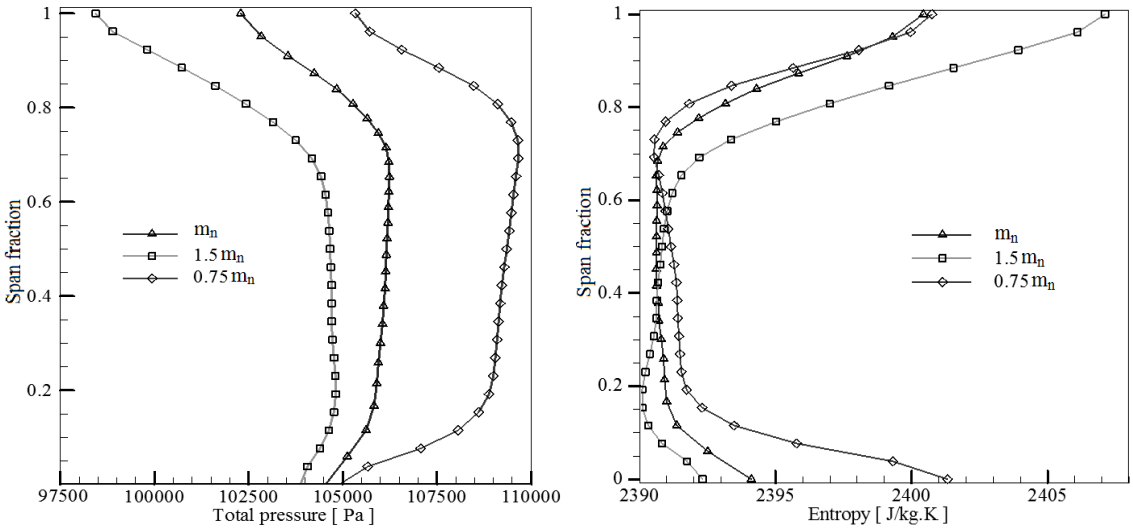

Figure 8 Spanwise distribution at the rotor exit: a) Total pressure; b) Entropy

Indeed, the wakes convected downstream of IGV and blades in addition to the secondary flows at hub and casing are major sources of entropy creation. The wakes issued from IGV (Fig. 9) are distorted in the hub corner of rotor blade due to secondary vortex formed from the suction side which is dissipated until about one third of span. Also, another vortex structure exists near the casing which rotates opposite to the tip flow leakage vortex. The maximum of entropy is associated with the rotor blade tip flow leakage and the tip vortex. Both IGV wakes and separations observed in the inter-row spacing are convected through the rotor blades passages, appearing not fully mixed at the rotor exit.

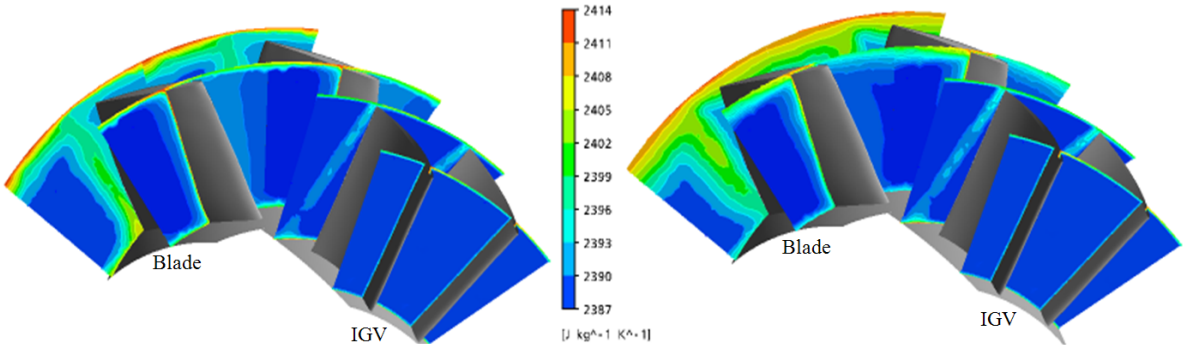

(a) **(b)**

Figure 9 Static entropy at different cross sections along the fan stage: a) nominal point: b); reduced mass flow (70%) point

3.3 Effect of axial inter-distance

For large axial inter-distance (Fig. 10) the axial flow velocity is quite uniform downstream IGV vanes, even at low flow rates. If this gap is reduced further an important blockage is observed from mid-span to tip sections of blade, hence concentrating the flow toward the lower part of blade. This blockage induced by the proximity of IGV and blades is related to the aerodynamic loadings over the suction sides and the overturning of flow streamlines. Meanwhile, this blockage causes alteration of flow incidence which reduces from hub to mid-span while increases from mid-span to blade tip, and subsequently inducing high losses.

Received:Added at production | Revised:Added at production | Accepted: Added at production
DOI: xxx/xxxx

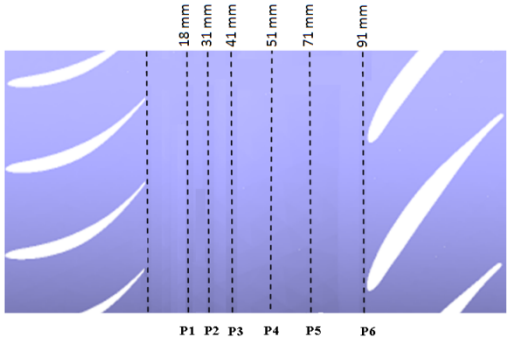

Figure 10 Axial inter-distances

Figure 11 shows the profiles of total pressure at exit from IGV and near the leading edge of blade for different inter-distances, revealing distinguishable differences between the small and large gaps. Indeed, for small inter-distances, positions (P1, P2), there are additional losses produced between blade span 30 % and 70 % compared to the large inter-distance such as the position (P3), subsequently the fan stage produces low aerodynamic efficiency. Another reason is that the IGV wakes do not completely mix prior to entering the blades passages in case of a small axial gap. The IGV wakes entering the blades passage influence the boundary layer to cause transition to turbulent flow sooner than if the wakes were allowed to mix sufficiently, which results in greater entropy production. Moreover, the tip vortex does not reach the blade span below 80 % for the farthest inter-distances, whereas for the closest inter-distances the tip vortex may reach at around 40 % span because it drifts to the lower spans. The greater strength of leakage flow for the closest spacing over the farthest case may be another reason that the vortex is able to influence the mid-span region. At the farthest position (P6) the total pressure profile varies greatly with blade span, with a clear defect in the total pressure below the span fraction 40 % where there is a noticeable shift along the span due to more losses attributed to IGV wakes mixing within the rotor passages. As also noticed the streamlines showed the tendency of IGV wakes to drift toward the rotor blades pressure side. The present results concur well with the assessment of Hetherington and Moritz [29] and Zachcial and Nürnberger [30] who have shown that the axial inter-distance between the blade rows allows for mixing prior entering the rotor passage. Due to wake mixing losses, Hetherington and Moritz [29] have suggested that blades-rows should be spaced far enough apart to allow for the majority of the mixing to be accomplished. In the present study the effect of inter-distance on the performance of axial fan stage in term of total-to-total isentropic efficiency was computed and assessed at the nominal operating speed. As presented in Fig. 12, there is a large variation in total-to-total isentropic efficiency with inter-distance. Accordingly, the maximum efficiency of 78.81% corresponds to the optimum inter-distance of 40 mm based on 61.5 % of the IGV chord and 44.5 % of the rotor blade chord. Above this distance the efficiency decreases noticeably. Indeed, the small axial inter-distance seems to strengthen the recovery of wake decay and then reduces the mixing losses of wakes, so did the total pressure loss. The efficiency obtained in conditions of reduced axial inter-distance is higher than that obtained corresponding to increased axial gap beyond the optimum distance.

Received:Added at production | Revised:Added at production | Accepted: Added at production
DOI: xxx/xxxx

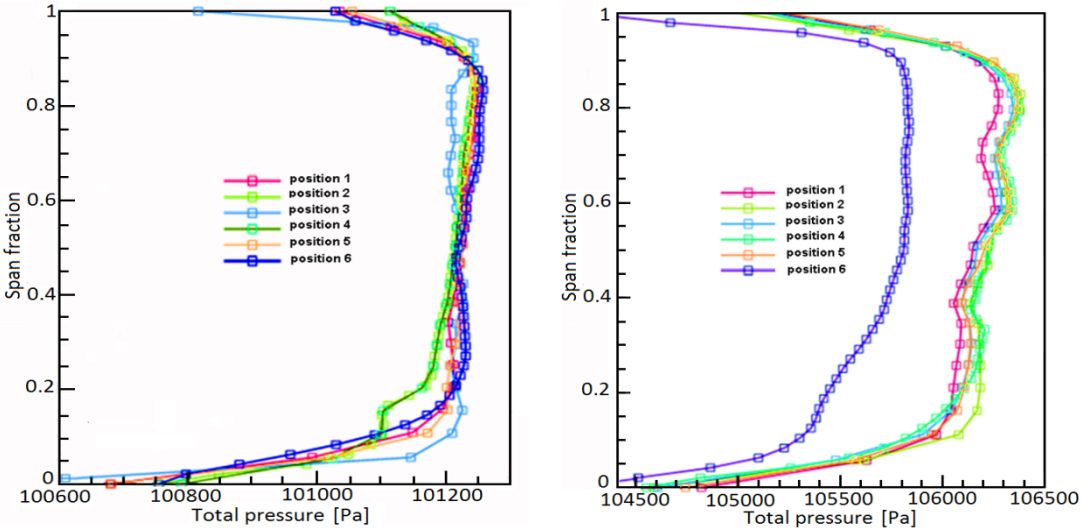

(a) **(b)**

Figure 11 Variations of total pressure at: a) exit of IGV, b) near leading edge of rotor blade

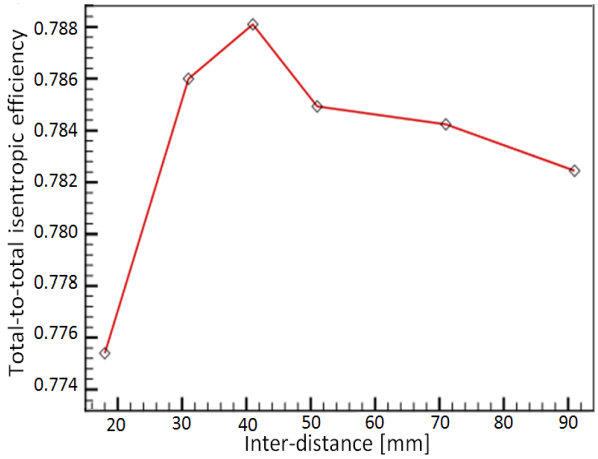

Figure 12 Total-total isentropic efficiency vs. axial inter-distance

5 | UNSTEADY FLOW ANALYSIS

The transient relative motion on each side of GGI connection was simulated and the interface position updated at each time step. The high-resolution advection scheme and second order backward Euler transient scheme were used. For every time step ten internal coefficient loops were selected and the pressure was monitored at the same spatial locations. In this section the expected dominant modes and frequencies and the sequence of interactions were determined analytically, followed by a characterization of the pressure fluctuations computed and recorded at several monitor points. The development of instabilities negatively affects the overall operating performance of axial fan stage which could be alleviated by understanding the unsteady flow interactions. Also it is useful to know the modal frequencies to ensure that any applied periodic loading frequency does not induce resonance leading to large oscillations. This section addresses the unsteadiness arising from both periodic (correlated with speed of rotation) and non-periodic fluctuations induced by RSI.

Received:Added at production | Revised:Added at production | Accepted: Added at production
DOI: xxx/xxxx

5.1 Expected modes of interactions

The components interactions are important sources of pressure fluctuations and vibrations in turbomachinery. It is therefore useful to know the modal frequencies in respect of the resonance leading to operation instability and fatigue of blades. The n^{th} blade passing in front of the m^{th} vane receives the same fluid force as passing in front of the next $(m+1)^{th}$ vane, and after an entire revolution the n^{th} blade receives N_s times the same force [31]. Also, for a number of blades N_r and vanes N_s, after an entire revolution each blade receives N_s times the same fluid force. The blade takes $2\pi/\Omega$ for completing an entire revolution and receives a repetitive force with a period $T_s = 2\pi/\Omega N_s$, and thus the resulting force over the blades related to RSI could be described by the Fourier series [32], as follows:

$$f_n = \sum_i F_{i,n}\, sin(iN_s\Omega t - \emptyset_{in}) \tag{8}$$

During an entire revolution each of N_r blades interacts with all $N_s$vanes so that there are a total of N_sN_r interactions separated by an angle $\Delta\theta_{RSI} = (1/N_s - 1/N_r)$ which in our case $\Delta\theta_{RSI} = 0.03827\, rad$. The time $\Delta t_{RSI} = 2\pi/(N_rN_s\Omega)$= $47.84\ \mu s$ for a rotating speed of 6000 rpm. The phase difference between two consecutive interactions is constant for the same harmonic [33]. For a given frequency $f = \Omega/2\pi$ occurring after an angular rotation equivalent to Δt_{RSI} the order of interaction depends on the first position of blade [32, 34, 35]. The sequences of interactions between 19 vanes and 11 blades are listed in Table 2. By considering that the 1st vane first interacts with the 1st blade, the sequence of interactions depicts that one blade interacts with another vane after $11\Delta t_{RSI}$ and the 1st blade interacts again with the 1st vane after $209\Delta t_{RSI}$.

Table 2. Order of interaction of 19 vanes with 11 blades, at t=0 the 1st blade is near 1st vane

$i.\Delta t_{RSI}$	0	1	2	3	4	5	6	7	8	9	10	11	12	13	14	15	16	17	18	19
blade	1	5	9	2	6	10	3	7	11	4	8	1	5	9	2	6	10	3	7	11
vane	1	8	15	3	10	17	5	12	19	7	14	2	9	16	4	11	18	6	13	1
$i.\Delta t_{RSI}$	20	21	22	23	24	25	26	27	28	29	30	31	32	33	34	35	36	37	38	39
blade	4	8	1	5	9	2	6	10	3	7	11	4	8	1	5	9	2	6	10	3
vane	8	15	3	10	17	5	12	19	7	14	2	9	16	4	11	18	6	13	1	8
$i.\Delta t_{RSI}$	40	41	42	43	44	45	46	47	48	49	50	51	52	53	54	55	56	57	58	59
blade	7	11	4	8	1	5	9	2	6	10	3	7	11	4	8	1	5	9	2	6
vane	15	3	10	17	5	12	19	7	14	2	9	16	4	11	18	6	13	1	8	15
$i.\Delta t_{RSI}$	60	61	62	63	64	65	66	67	68	69	70	71	72	73	74	75	76	77	78	79
blade	10	3	7	11	4	8	1	5	9	2	6	10	3	7	11	4	8	1	5	9
vane	3	10	17	5	12	19	7	14	2	9	16	4	11	18	6	13	1	8	15	3
$i.\Delta t_{RSI}$	80	81	82	83	84	85	86	87	88	89	90	91	92	93	94	95	96	97	98	99
blade	2	6	10	3	7	11	4	8	1	5	9	2	6	10	3	7	11	4	8	1
vane	10	17	5	12	19	7	14	2	9	16	4	11	18	6	13	1	8	15	3	10
$i.\Delta t_{RSI}$	100	101	102	-	-	-	-	-	-	-	-	-	-	-	-	-	-	207	208	209
blade	5	9	2	-	-	-	-	-	-	-	-	-	-	-	-	-	-	4	8	1
vane	17	5	12	-	-	-	-	-	-	-	-	-	-	-	-	-	-	6	13	1

The non-uniform flow field at the exit of vanes caused by wakes and blade loading generate a periodic flow pattern [36]. The induced pressure wave rotates at the same runner speed and thus the characteristic pressure oscillation has a frequency $f_s = m\frac{\Omega}{2\pi}N_r$ at every stationary

Received:Added at production | Revised:Added at production | Accepted: Added at production
DOI: xxx/xxxx

point and $f_r = n\frac{\Omega}{2\pi}N_s$ at every rotating point. The common action of the rotating and stationary fields gives rise to $N_r N_s$ pressure impulses per a revolution [31]. The flow field leaving the distributor vanes (Figure 13) is characterized by a velocity defect and the pressure field attached to the runner blades induces to the incoming flow field distortions.

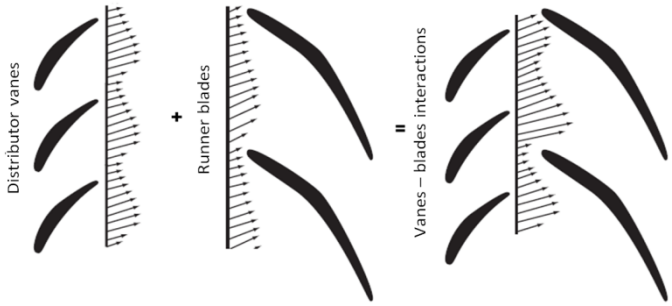

Figure 13 illustration of the process of modulation (adapted from [37])

The pressure field combining both the vanes and blades pressure fields is characterized by a modulation process representing the interactions which by considering $\theta_s = \theta_r + \Omega t$ may be expressed according to Franke et al. [35] by:

$$p_{m,n}(\theta_s, t) = \frac{A_{mn}}{2}\cos[mN_r\Omega\mathrm{t} - (mN_r - nN_s)\theta_s + \emptyset_n - \emptyset_m] + \frac{A_{mn}}{2}\cos[mN_r\Omega\mathrm{t} - (mN_r + nN_s)\theta_s - \emptyset_n - \emptyset_m] \quad (9)$$

A_{mn} is a combined pressure amplitude due to interaction of each harmonic. This pressure field presents two diametrical pressure modes $k_1$and k_2 which indicate the number of high-pressure and low-pressure regions for a frequency component in the circumferential direction [38]:

$$k_1 = m\mathrm{N_r} + n\mathrm{N_s} \quad \text{and} \quad k_2 = m\mathrm{N_r} - n\mathrm{N_s} \quad (10)$$

The sign of the diametrical mode numbers k_1 and k_2 indicates that the diametrical mode is rotating in the same direction as the runner when is positive, while a negative value indicates a counter-rotation with a spinning speed $(\omega, \dot{\omega})$ [31].

$$\omega_1 = mN_r\Omega/k_1 \quad \text{and} \quad \omega_2 = mN_r\Omega/k_2 \quad (11a)$$
$$\dot{\omega_1} = nN_s\Omega/k_1 \quad \text{and} \quad \dot{\omega_2} = nN_s\Omega/k_2 \quad (11b)$$

As noted the low amplitudes are expected for high k values because of high harmonic number and k_1 is usually not relevant.

The runner blades 1, 2, 3…. and 11 are first excited by interference with the vanes' wakes. Runner blades are excited in phase and induce a vibration having a mode with 2 diametrical nodes. The runner provokes a pressure wave rotating at the same runner speed, inducing a characteristic pressure oscillation of frequency $f_s = m\frac{\Omega}{2\pi}N_r$ and $f_r = n\frac{\Omega}{2\pi}N_s$ at every stationary/rotating point. The pressure field presents two diametrical pressure modes k_1, k_2 indicating the number of high- and low-pressure regions for the frequency component in the circumferential direction estimated in Table 3 for a combination of 19 vanes and 11 blades. When operating at 6000 rpm, the highest RSI calculated diametrical positive mode number (Table 4) occurs for k_2=3, 14, 25, 36, 47, 58, 69, 80, 91, and 102 for the successive frequency

Received:Added at production | Revised:Added at production | Accepted: Added at production
DOI: xxx/xxxx

2200 Hz, 3300 Hz, 4400 Hz, 5500Hz, 6600 Hz, 7700 Hz, 8800 Hz, 9900 Hz, 11000 Hz, and 12100 Hz. The highest RSI calculated diametrical negative mode number (Table 5) occurs for k_2 = -8, -16, -5, -13, -2, -10, -18, -7, -15, -4 and -12 for the successive frequency 1100 Hz, 2200 Hz, 3300 Hz, 4400 Hz, 5500Hz, 6600 Hz, 7700 Hz, 8800 Hz, 9900 Hz, 11000 Hz and 12100 Hz. This theoretical analysis allow describing the characteristics of pressure mode shape in the frequency domain and the sequences of interactions which may give the expected dominant modes and frequencies, however it is difficult to predict accurately the amplitudes in addition to other interactions frequencies.

Table 3. Sample of expected RSI diametrical mode numbers and frequencies

m	n	k_1	k_2	ω_1/Ω	ω_2/Ω	f_s/f	f_s	$\grave{\omega}_1/\Omega$	$\grave{\omega}_2/\Omega$	f_r/f	f_r
1	1	30	-8	0.3667	-1.375	11	1100	0.633	-2.375	19	1900
1	2	49	-27	0.2245	-0.4074	11	1100	0.776	-1.407	38	3800
1	3	68	-46	0.1618	-0.2391	11	1100	0.838	-1.239	57	5700
-	-	-	-	-	-	-	-	-	-	-	-
2	1	41	3	0.5366	7.3333	22	2200	0.463	6.333	19	1900
2	2	60	-16	0.3667	-1.375	22	2200	0.633	-2.375	38	3800
2	3	79	-35	0.2785	-0.6286	22	2200	0.722	-1.629	57	5700
-	-	-	-	-	-	-	-	-	-	-	-
3	1	52	14	0.6346	2.3571	33	3300	0.365	1.357	19	1900
3	2	71	-5	0.4648	-6.6	33	3300	0.535	-7.6	38	3800
3	3	90	-24	0.3667	-1.375	33	3300	0.633	-2.375	57	5700
-	-	-	-	-	-	-	-	-	-	-	-
4	1	63	25	0.6984	1.76	44	4400	0.302	0.76	19	1900
4	2	82	6	0.5366	7.3333	44	4400	0.463	6.333	38	3800
4	3	101	-13	0.4356	-3.3846	44	4400	0.564	-4.385	57	5700
-	-	-	-	-	-	-	-	-	-	-	-
5	1	74	36	0.7432	1.5278	55	5500	0.257	0.528	19	1900
5	2	93	17	0.5914	3.2353	55	5500	0.409	2.235	38	3800
5	3	112	-2	0.4911	-27.5	55	5500	0.509	-28.5	57	5700
-	-	-	-	-	-	-	-	-	-	-	-
6	1	85	47	0.7765	1.4043	66	6600	0.224	0.404	19	1900
6	2	104	28	0.6346	2.3571	66	6600	0.365	1.357	38	3800
6	3	123	9	0.5366	7.3333	66	6600	0.463	6.333	57	5700
-	-	-	-	-	-	-	-	-	-	-	-
7	1	96	58	0.8021	1.3276	77	7700	0.198	0.328	19	1900
7	2	115	39	0.6696	1.9744	77	7700	0.33	0.974	38	3800
7	3	134	20	0.5746	3.85	77	7700	0.425	2.85	57	5700
-	-	-	-	-	-	-	-	-	-	-	-
8	1	107	69	0.8224	1.2754	88	8800	0.178	0.275	19	1900
8	2	126	50	0.6984	1.76	88	8800	0.302	0.76	38	3800
8	3	145	31	0.6069	2.8387	88	8800	0.393	1.839	57	5700
-	-	-	-	-	-	-	-	-	-	-	-
9	1	118	80	0.839	1.2375	99	9900	0.161	0.237	19	1900
9	2	137	61	0.7226	1.623	99	9900	0.277	0.623	38	3800
9	3	156	42	0.6346	2.3571	99	9900	0.365	1.357	57	5700
-	-	-	-	-	-	-	-	-	-	-	-
10	1	129	91	0.8527	1.2088	110	11000	0.147	0.209	19	1900
10	2	148	72	0.7432	1.5278	110	11000	0.257	0.528	38	3800
10	3	167	53	0.6587	2.0755	110	11000	0.341	1.075	57	5700
-	-	-	-	-	-	-	-	-	-	-	-

Received:Added at production | Revised:Added at production | Accepted: Added at production
DOI: xxx/xxxx

Table 4. Main expected RSI diametrical positive mode k_2 and frequency

k_1	k_2	ω_1/Ω	ω_2/Ω	f_s/f	f_s
41	3	0.5366	7.3333	22	2200
52	14	0.6346	2.3571	33	3300
63	25	0.6984	1.76	44	4400
74	36	0.7432	1.5278	55	5500
85	47	0.7765	1.4043	66	6600
96	58	0.8021	1.3276	77	7700
107	69	0.8224	1.2754	88	8800
118	80	0.839	1.2375	99	9900
129	91	0.8527	1.2088	110	11000
140	102	0.8643	1.1863	121	12100

Table 5. Main expected RSI diametrical negative mode k_2 and frequency

k_1	k_2	ω_1/Ω	ω_2/Ω	f_s/f	f_s
30	-8	0.3667	-1.375	11	1100
60	-16	0.3667	-1.375	22	2200
71	-5	0.4648	-6.6	33	3300
101	-13	0.4356	-3.3846	44	4400
112	-2	0.4911	-27.5	55	5500
142	-10	0.4648	-6.6	66	6600
172	-18	0.4477	-4.2778	77	7700
183	-7	0.4809	-12.5714	88	8800
213	-15	0.4648	-6.6	99	9900
224	-4	0.4911	-27.5	110	11000
254	-12	0.4764	-10.0833	121	12100

5.2 Analysis of unsteady pressure field

Unsteady simulations were carried out for the fan operating at the nominal point considering the transient-rotor-stator interface and a time step of $41.66\,\mu s$, which is adequate for capturing the effect of the relative motion. The static pressure fluctuations for one rotor revolution are invariant with the reference frame and were recorded at monitor positions at 10 %, 50 % and 90 % of span of IGV/rotor interface and at the rotor/outlet interface as seen from Fig. 14. Pressure fluctuation and spectrums shown by Figs. 15(a-c) depict 11 lobs corresponding to the blades count, where the first peak corresponds to the fundamental blade passing frequency (BPF) $f_s = m\frac{\Omega}{2\pi}\mathrm{N_r} = 1\frac{6000}{60}\frac{1}{2\pi} = 1100$ Hz. The harmonics of the pressure signal corresponding to multiples of the fundamental frequency are embedded in the broad band of the frequency domain are suitably predicted. The spectrum is mainly connected with the fundamental harmonic (1100 Hz) and its multiples, and it would be logical to have essentially this principal one in case of a single row. The main peaks at the frequency of 1100 Hz and 2200 Hz are also predicted according to Table 4 and 5. Another peak of lower amplitudes related to IGV wake occurs at frequencies multiple of 1900 Hz. The pressure fluctuation related to the potential effect related to blade movement is propagating both upstream and downstream in the form of pressure wave. One could observe a great variation of pressure fluctuations between the points located at interface IGV/rotor and at rotor /outlet, which the amplitudes tend to decrease downstream of rotor blades (Fig. 16). Near the leading edge of rotor blades BPF is always the dominant structure while moving away the potential mode of interaction is dumped either downstream or upstream. Figure 16 illustrates the existence of other modes of different amplitudes superimposed related to wakes interaction from IGV and rotor as well as the secondary flows and tip vortices. A comparison between

Received:Added at production | Revised:Added at production | Accepted: Added at production
DOI: xxx/xxxx

the harmonics indicates high peaks at 90 % of span followed by those obtained near hub, whereas the moderate amplitudes are seen at mid-span. Besides, the most disturbed region is characterized by the highest amplitude as it is influenced by the vortex structures near the blade tip and the secondary flow near the nub.

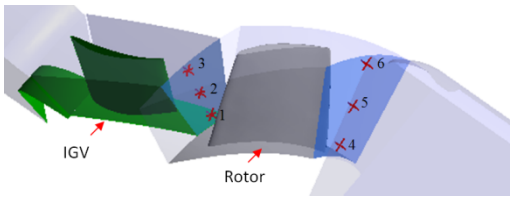

Figure 14 Monitor points of pressure fluctuations

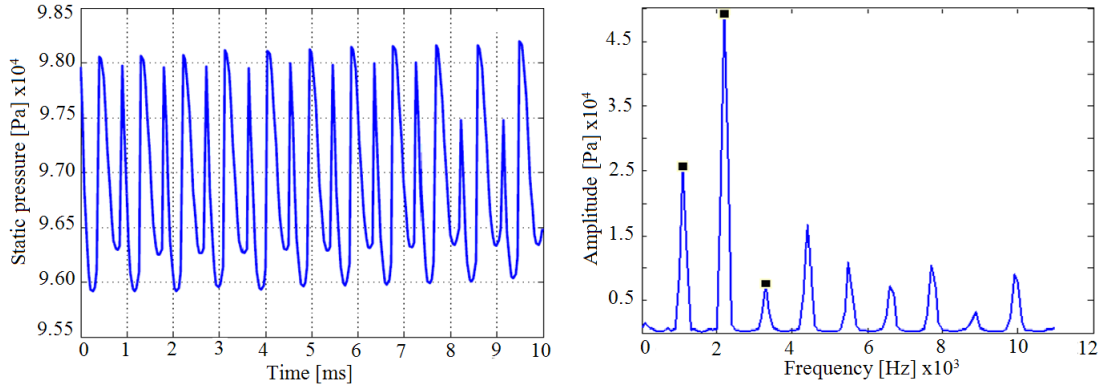

(a)

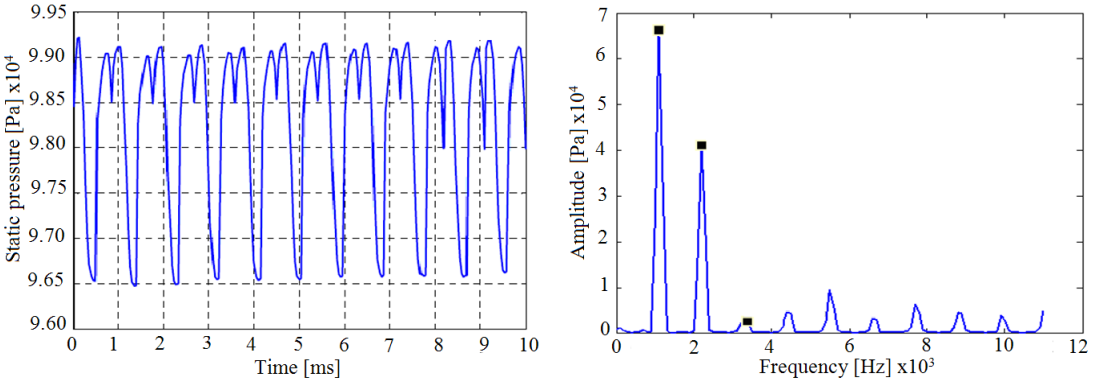

(b)

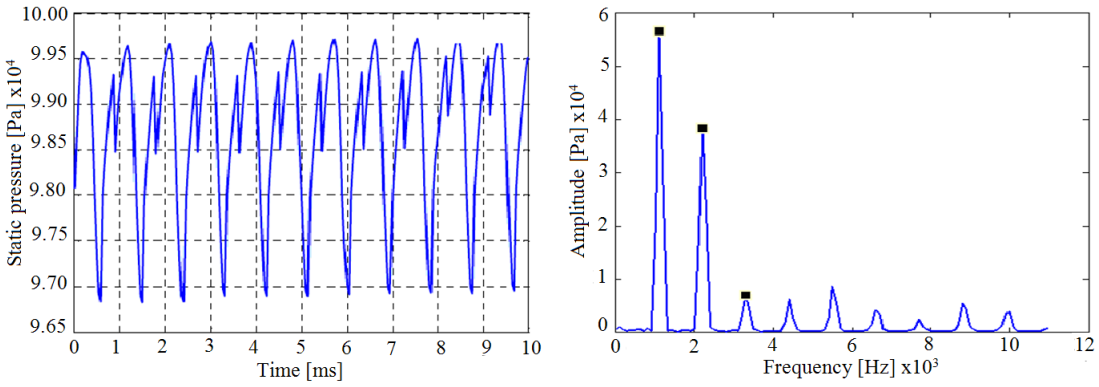

(c)

Fig. 15 Pressure fluctuations and FFT at different span of IGV/rotor interface: a) 10%, b) 50 % and c) 90 %

Received:Added at production | Revised:Added at production | Accepted: Added at production
DOI: xxx/xxxx

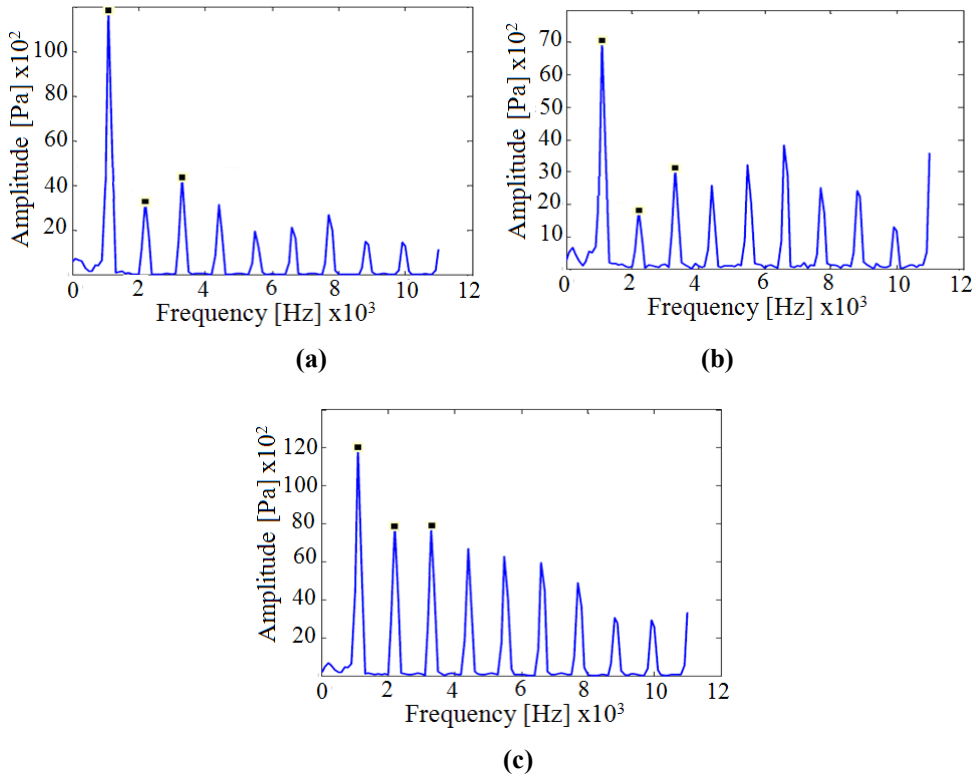

Fig. 16 FFT at rotor/outlet interface at span 10% (left), 50% (middle) and 90% (right)

In this IGV-rotor configuration the main unsteadiness is attributed to the core of rotor wakes, and the intensity of velocity deficit in wakes is modulated by the unmixed vanes wakes convected out in the rotor passages. The behavior of this deterministic unsteadiness is seen to be more important at low flow rates operation. To examine the effects of pseudo IGV clocking, the vane was displaced at four positions. Table 6 summarizes the obtained amplitudes of pressure fluctuations at IGV/ rotor interface. As noticed the amplitude of the principal mode and its harmonics are sensitive; for reference position and that of 4.73 deg and 18.95 deg, the potential mode and harmonics are seen the dominant, whereas for positions of 9.47 deg and 14.21 deg, there is an emergence of a second mode with a frequency 2200 Hz which becomes very important. These pseudo interactions depend on the clocking angle as highlighted by amplitudes of predominance modes.

Table 6. Pressure amplitude of main frequencies at IGV/Rotor interface with pseudo clocking positions

Frequency →		1100	2200	3300	4400	5500	6600	7700	8800	9900	11000
Position	Recording points	Amplitude (Pa)									
0 deg	10%	70074	26138	9374	3414	4196	5936	3702	1541	2872	4032
	50%	72924	17535	6214	1927	3653	2218	1887	947	556	766
	90%	82372	15384	4775	1617	509	173	683	278	147	210
4.73 deg	10%	30448	50031	8397	16894	11195	7824	10650	2542	9561	807
	50%	66289	39729	2150	7248	9632	2663	6216	4069	3411	4931
	90%	22135	37798	5749	6421	7808	3888	2329	5410	3762	572
9.47 deg	10%	25690	49178	7747	16616	10935	7177	10403	2267	9012	861
	50%	66437	40957	3401	7706	9474	3176	6275	4328	3806	4752
	90%	56567	38418	6896	6109	8547	4182	2379	5340	3565	810

Received:Added at production | Revised:Added at production | Accepted: Added at production
DOI: xxx/xxxx

4.21	10%	59853	4470	7789	4215	3622	3184	2369	-	-	-
deg	50%	66152	12521	966	2241	1413	1103	947	610	-	-
	90%	82528	15434	4552	1692	560	298	540	154	103	115

5.3 Effect of Axial inter-distance

IGV wake requires a greater mixing-out for a large axial inter-distance which facilitates convection; on the contrary the wakes introduce a considerable discontinuity into the velocity field for the small inter-distance. As there is tangential fluctuation in the structure of the blockage, and that means the tangential uniformity of the flow is broken by IGV wakes discontinuities, a clear interaction between IGV wakes and periodic blockage of the rotor blades occurs. The reduction in inter-distance produces a clear spanwise redistribution of flow velocity, with blockage pattern from mid-span to blade tip; so the flow is concentrated near the hub. Moreover, the defect related to IGV wakes is greater in the case of reduced inter-distance, because of the inherent non-uniform flow pattern. Near the tip there is an important reduction in axial velocity caused by the rotor blockage which is more extreme when IGV wakes occur in particular angular positions as seen before. To assess the effect of inter-distance six gaps were considered for the unsteady flow simulations while recording the static pressure at IGV/rotor interface. Table 7 shows that the amplitude of fundamental harmonic of 1100 Hz has maximum amplitude at the minimum distance but amplitude is less for larger inter-distance. It seems that the amplitudes of pressure fluctuations recorded at points (P1, P2 and P3) tend to decrease almost proportionally to the inverse of distance and this trend is maintained until the optimal distance; afterwards the amplitude of points (P2 and P3) rises again, but slightly for the point (P1) which afterwards varies moderately for large inter-distance but depending on the monitor point location. The amplitude of second harmonic of 2200 Hz varies significantly with inter-distance, while the minimum is still occurring around the optimum position. The monitor point at the mid-span has smaller fluctuations in pressure. However, for the third harmonic of frequency 3300 Hz, the amplitude seems varying significantly to reach a minimum and then increases slightly, afterwards drops for the large inter-distance. It appears that almost all the harmonics produce the minimum fluctuations of pressure around the optimum distance as depicted in Fig 17. Finally, it seems that the potential interaction appearing in the form of periodic pressure fluctuations propagating both upstream and downstream of blade-row becomes dominant for small axial inter-distance for this large pitch by chord ratio axial fan stage compared to an axial compressor.

Table 7. Pressure amplitude for main frequencies at IGV/rotor interface with axial inter-distance

Frequency →		1100	2200	3300	4400	5500	6600	7700	8800	9900	11000
Axial gap	Recording points	Amplitude (Pa)									
18	10%	140820	46240	20830	7800	4280	4380	2820	3220	2940	2310
mm	50%	156720	42710	18340	9770	4340	1660	890	170	290	210
	90%	136240	26130	7000	7280	7660	5650	5200	4580	4620	4020
26	10%	76546	51361	11080	17514	3035	8516	2242	5423	2579	4560
mm	50%	116820	69840	4350	7000	14570	8890	5180	7360	6690	4650
	90%	103100	5866	3446	2973	2653	1386	547	769	1246	1358
31	10%	31422	52775	6953	17605	9908	7648	10440	2433	8961	1164
mm	50%	65261	42814	3866	8196	10528	2908	6783	4684	3691	4983

Received:Added at production | Revised:Added at production | Accepted: Added at production
DOI: xxx/xxxx

	90%	57477	42630	6583	7383	10112	5201	2855	6797	4752	736
41 mm	10%	20540	8790	5221	3329	-	-	-	-	-	-
	50%	49599	8886	8290	5484	4082	-	-	-	-	-
	90%	51936	15072	5965	4733	3569	2620	-	-	-	-
51 mm	10%	41279	48706	21620	18091	18402	8396	14227	10825	7138	11397
	50%	44390	39736	5678	24912	15231	12789	4261	2510	18	7121
	90%	58769	55103	24347	19263	7789	10090	15456	4250	6005	13899
71 mm	10%	24235	45908	8264	16157	10708	7353	9923	2390	8689	814
	50%	63439	39943	2688	7102	9630	2955	6582	4288	3339	4790
	90%	57705	39286	7686	6272	8325	4448	2537	5358	3615	482
91 mm	10%	21706	9215	5514	3492	-	-	-	-	-	-
	50%	51612	9330	8441	5773	4188	-	-	-	-	-
	90%	49980	14969	5505	4249	3052	2192	-	-	-	-

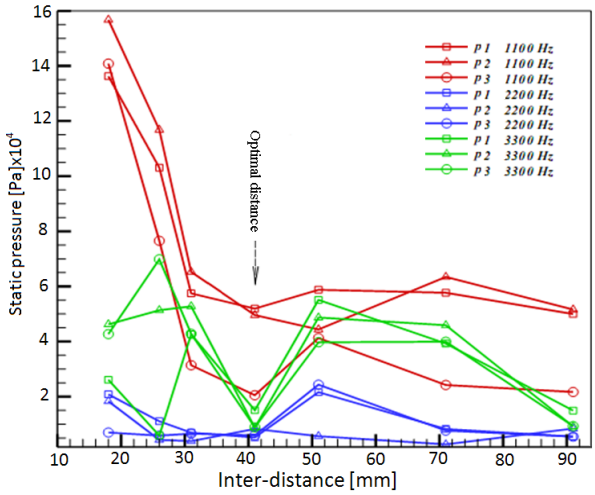

Figure 17. Amplitude of pressure fluctuations for main harmonics vs. inter-distance

6 | CONCLUSION

The aerodynamic characteristics of a high-speed high-reaction pre-whirl axial fan stage are determined. The variation of axial inter-distance has revealed an optimum spacing allowing for the majority of wake diffusing and mixing and subsequently reaching a maximum aerodynamic efficiency. The steady flow simulations have shown that the model of frozen IGV/rotor interface has a weak influence on the average flows and the pseudo interactions. Better results, including RSI, are obtained from the unsteady flow simulation based on the frozen-rotor interface. Time mode analysis of pressure fluctuations has permitted the determination of different frequencies and the prevailing modes of a lobed structure of pressure waves. The amplitudes of pressure fluctuations and harmonics are shown to vary significantly depending on the monitor locations and also on the axial inter-distance. It is clear that IGV/rotor interactions are influenced by this distance, and the potential interaction propagating upstream and downstream of blade-row prevails more for the small inter-distances. Accordingly, an optimum distance has been identified which to maximizes the efficiency and minimize static pressure fluctuations which in turn may alleviate the levels of vibration and noise. More details about the vortical structures involvement in RSI studies requires adopting LES simulation but this is still requiring powerful computing resources.

Received:Added at production | Revised:Added at production | Accepted: Added at production
DOI: xxx/xxxx

DECLARATION OF CONFLICTING INTERESTS

The author(s) declared no potential conflicts of interest with respect to the research, authorship and/or publication of this article.

FUNDING

The author(s) received no financial support for the research, authorship and/or publication of this article.

ORCID

Adel-Ghenaiet: https://orcid.org/0000-0001-5112-3551

NOTATIONS

BPF = blade (or vane) passing frequency
c = chord
k_1, k_2 = excited diametrical modes
f = frequency (Hz);
N = vane or blade count;
N = rotational speed (rpm);
p = static pressure (Pa);
m = mass flow rate (kg/s);
η = aerodynamic efficiency;
Ω = angular velocity (rad/s);
ω = mode angular velocity (rad/s);
ρ = density (kg/m^3);
μ = dynamic viscosity (kg.m^{-1}.s^{-1});
θ = angular position (rad);
Subscripts
r = rotating domain
s = stationary domain

REFERENCES

[1] Kemp, R.H., Hirschberg, M.H. and Morgan, W.C. (1958) "Theoretical and experimental analysis of the reduction of rotor blade vibration in turbomachinery through the use of modified stator vane spacing", NACA, Technical Note 4373, (1958)

[2] Giles, M.B. (1987), "Calculation of unsteady wake/rotor interactions", AIAA Paper 87-006, 25th Aerospace Sciences Meeting, Reno, Nevada, 1987.

[3] Rai, M.M. (1987), "Navier-Stokes simulations of rotor/stator interaction using patched and overlaid grids", *J. of Propulsion and Power*, **3**, No. 5, pp. 387-396.

[4] Rai, K.V., Delaney, R.A. (1992), "Investigation of unsteady flow through a transonic turbine stage, Part I, Analysis", AIAA Paper No. 90-2408.

[5] Giles, M., Haimes, R. (1993), "Validation of a numerical method for unsteady flow calculation", *ASME J. of Turbomachinery*, 115, pp. 110-117.

[6] Arnone, A., Pacciani, R. (1996), "Rotor-stator interaction analysis using the Navier-Stokes equations and a multigrid method", *ASME J. of Turbomachinery,* 118, pp 679-689

[7] Yang J., Qiao W.Y, Shi P.J, Wang P.W. (2012) "Primitive staged stator solidity of axial

flow turbine to the rotor-stator interaction effects", *Journal of Aerospace Power*, 27(8):1832-1840

[8] Adamczyk, J.J., Celestina, M.L., Chen, J.P. (1996), "Wake-induced unsteady flow: their impact on rotor performance and wake rectification", *ASME Journal of Turbomachinery*, Vol. 118 January 1996, pp. 88 – 95

[9] Gallus H. E. (1998), "Experimental investigation of rotor-stator interaction in axial-flow turbines and compressors", *International Journal of Rotating Machinery* 1998, Vol. 4, No. 4, pp.217-231

[10] Kerrebrock J.L. , Mikolajczk A.A. (1970), "Intra-stator transport of rotor wakes and its effect on compressor performance", *ASME Journal of Engineering for Power*, Vol.92, pp 359-368.

[11] Binder, A, Forster, W., Kruse, H., Rogge, H. (1985), "An Experimental investigation into the effect of wakes on the unsteady turbine rotor flow", ASME Journal of Engineering for Gas Turbines and Power, Vol. 107, pp. 458-466,

[12] Hodson, H.P. (1985), "Measurements of wake generated unsteadiness in the rotor passages of axial flow turbines", *ASME J. Eng. Gas Turbines Power*, 107, pp. 337–344, 1985.

[13]] Hsu, S.T. , Wo, A.M. (1998), "Reduction of unsteady blade loading by beneficial use of vortical and potential disturbances in an axial compressor with rotor clocking", *ASME Journal of Turbomachinery*, 120, (1998), 705-713.

[14]] Lee, Y., Feng, J. (2004), "Potential and viscous interactions for a multi-blade-row compressor", *ASME Journal of Turbomachinery*, 126, (2004), 464-472.

[15] Mailach, R., Vogeler, K. (2004), "Rotor-stator interactions in a four-stage low-speed axial compressor - Part I: Unsteady profile pressures and the effect of clocking", *ASME Journal of Turbomachinery*, 126, (2004), 507-518.

[16] Mailach, R., Muller, L. and Vogeler, K. (2004), "Rotor-stator interactions in a four-stage low-speed axial compressor - Part II: Unsteady aerodynamic forces of rotor and stator blades". *ASME Journal of Turbomachinery*, 126, (2004), 519-526.

[17] Jia, H., Vogeler, K., Muller, L., Mailach, R. (2007), "Numerical investigation of rotor-stator interactions in a 1.5-stage low-speed axial compressor", *Journal of Computational and Applied Mechanics*, Vol. 8, No. 1, (2007), pp. 71/83

[18] Tsuchiya, N., Nakamura, Y., Yamagata, A., and Kodama, H., Nozaki, O., Nishizawa, T., Yamamoto, K., (2002) "Fan Noise Prediction Using Unsteady CFD Analysis", AIAA-2002-2491, 2002.

[19] Kodama, H., Yamagata, A., Tsuchiya, N., Nozaki, O., Nishizawa, T., Yamamoto, K. (2004),"CFD prediction of unsteady pressures due to fan rotor-stator interaction", ICAS 2004, 24TH International congress of the aeronautical sciences

[20] Oro, J. M.F., Argüelles Díaz, K.M., Morros, C. S., Tajadura, R. B. (2003), "Unsteady flow analysis of the stator-rotor interaction in an axial flow fan", Paper No. FEDSM2003-45394, ASME/JSME 2003 4th Joint Fluids Summer Engineering Conference, Honolulu, Hawaii, USA, July 6–10, 2003

[21] Oro, J. M.F., Argüelles Díaz, K.M., Morros C.S., Marigorta, E.B. (2007), "Unsteady flow and wake transport in a low-speed axial fan with inlet guide vanes", *J. Fluids Eng* 129(8), 1015-1029 (Mar 15, 2007) (15 pages)

[22] Vega, M.G., Oro, J. M.F., Argüelles Díaz, K.M., Morros, C.S. (2013),"Effect of rotor-stator configuration in the generation of vortical scales and wake mixing in single stage axial fans: Part I — LES Modelling and Experimental Validation", Paper No. FEDSM2013-16432, ASME 2013 Fluids Engineering Division Summer Meeting, 2013

[23] Menter, F.R. (1994), "Two-equation eddy-viscosity turbulence models for engineering applications", *AIAA Journal,* Vol. 32, No. 8, August 1994.

Received:Added at production | Revised:Added at production | Accepted: Added at production
DOI: xxx/xxxx

[24] Li, Z., Wang, Z., Wei, X., Qin, D. (2016), "Flow similarity in the rotor-stator interaction affected region in prototype and model Francis pump-turbines in generating mode", *ASME J. Fluids. Eng* 138 (2016) 15 pages.

[25] ANSYS CFX-Solver Theory Guide. Release 16.0. Canonsburg, USA. ANSYS Inc., 2015.

[26] Simpson, A.T., Spence, S.W.T., Watterson J.K. (2009), "Comparison of the flow structures and losses within vaned and vaneless stators for radial turbines", *ASME Journal of Turbomachinery*, July 2009, Vol. 131 / 031010-1.

[27] F. M. White, Fluid Mechanics, 5th edition, page 467. 2003

[28] Wilcox, D.C. (1994), "Simulation of transition with a two-equation turbulence model", *AIAA Journal*, Vol. 32, No. 2, Feb. 1994, pp. 247-255.

[29] Hetherington, R., Moritz, R.R., (1977), "The influence of unsteady flow phenomena on the design and operation of aero engines", Unsteady Flow Phenomena in Turbomachinery, AGARD CP 177

[30] Zachcial, A., Nürnberger, D., (2003), "A Numerical Study on the Influence of Vane-Blade Spacing on a Compressor Stage at Sub- And Transonic Operating Conditions", ASME Paper No. GT2003-38020

[31] C. Nicolet, N. Ruchonnet, S. Alligné, J. Koutnik and F. Avellan, "Hydroacoustic simulation of rotor-stator interaction in resonance conditions in Francis pump-turbine," 25th IAHR Symposium on Hydraulic Machinery and Systems IOP Publishing IOP Conf. Series: Earth and Environmental Science 12 (2010) 012005 doi:10.1088/1755-1315/12/1/012005

[32] C. G., Rodriguez, E. Egusquiza and I. F. Santos, "Frequencies in the Vibration Induced by the Rotor Stator Interaction in a Centrifugal Pump Turbine," ASME J. Fluids Eng., 2007, Vol. 129(11):1428-1435. doi: 10.1115/1.2786489

[33] I. Oftebroand and A. Lunning, "Pressure oscillations in Francis turbines," Proc Inst of Mech Engrs, vol 181, pp 119-124, 1966.

[34] C. Trivedi, M. J. Cervantes, B. K. Gandhi and O. G. Dahlhaug, "Experimental and Numerical Studies for a High Head Francis Turbine at Several Operating Points," ASME J. Fluids Eng, 2013, Vol. 135(11):111102-111102-17.FE-12-1618, doi: 10.1115/1.4024805

[35] G. Franke, C. Powell, U. Seidel, J. Koutnik and R. Fischer, "On Pressure Mode Shapes Arising from Rotor/Stator Interactions," Journal of Sound & Vibration. 39. 14-18. 2005.

[36] C. Nicolet, N. Ruchonnet, S. Alligné, J. Koutnik and F. Avellan, "Hydroacoustic simulation of rotor-stator interaction in resonance conditions in Francis pump-turbine," 25th IAHR Symposium on Hydraulic Machinery and Systems IOP Publishing IOP Conf. Series: Earth and Environmental Science 12 (2010) 012005 doi:10.1088/1755-1315/12/1/012005

[37] A. Zobeiri, J. L. Kueny, M. Farhat and F. Avellan, "Pump-Turbine Rotor-Stator Interactions in Generating Mode: Pressure Fluctuation in Distributor Channel," 23rd IAHR Symposium, Yokohama, Japan, Oct. 17–21, 2006

[38] J. M. Tyler and T. G. Sofrin, "Axial Flow Compressor Noise Studies," SAE Transactions, Vol. 70, pp. 309-332, 1962, https://www.jstor.org/stable/i40187906